

Analysis of the 2017 June Maoxian landslide processes with force histories from seismological inversion and terrain features

J. Zhao^{1,2}, C.J. Ouyang³, S.D. Ni^{1,2}, R.S. Chu² and A. Mangeney^{4,5}

¹School of Mechanical Engineering and Electronic Information, China University of Geosciences, Wuhan 430074, China. E-mail: zhaojuan@cug.edu.cn

²State Key Laboratory of Geodesy and Earth's Dynamics, Institute of Geodesy and Geophysics, Chinese Academy of Sciences, Wuhan 430077, China

³Key Laboratory of Mountain Hazards and Surface Process and Institute of Mountain Hazards and Environment, Chinese Academy of Sciences, Chengdu 610041, China

⁴Institut de Physique du Globe de Paris, CNRS-UMR7580, University Paris-Diderot, 75005 Paris, France

⁵ANGE Team, INRIA, Laboratory J. Louis Lions, 75252 Paris, France

Accepted 2020 May 26. Received 2020 March 12; in original form 2019 November 20

SUMMARY

A devastating landslide occurred in Maoxian (China) on 2017 June 24, which generated strong signals that were recorded by a regional seismic network. We determined the landslide force history from long-period seismic waves and identified eight subevents. For each subevent, we obtained an independent force history and calculated its sliding path. The shape of the terrain before and after the landslide was found to play a critical role in the motion of the sliding mass. A combination of seismic and terrain data was used to discriminate between or relate the subevents to each other, and to locate the initiation point of each sliding path. We explain the Maoxian landslide dynamics as the combination of the rock collapse, centripetal acceleration of the sliding body, deceleration and acceleration once again after overcoming obstacles along the sliding path.

Key words: Geomorphology; Time-series analysis; Waveform inversion.

1 INTRODUCTION

A landslide can be simplified as a block moving down a slope due to gravity and under friction. The key to studying the bulk movement of a sliding body is to determine a force model that conforms to the landslide characteristics (Kanamori & Given 1982; Kawakatsu 1989; Fukao 1995; Brodsky *et al.* 2003; Favreau *et al.* 2010), and to obtain the landslide dynamics through the inversion of low-frequency seismic signals (Lin *et al.* 2010; Moretti *et al.* 2012; Allstadt 2013; Ekström & Stark 2013; Yamada *et al.*, 2013, 2016, 2018; Hibert *et al.*, 2014, 2015, 2017; Iverson *et al.* 2015; Moretti *et al.* 2015; Zhao *et al.* 2015; Li *et al.*, 2017, 2019; Farin *et al.* 2018; Gualtieri and Ekström 2018; Schöpa *et al.* 2018). The force model, inverted from broad-band seismic waves, is usually a three-component force history that describes the forces imposed on the ground by the landslide. Using the force history and Newton's laws, it is possible to deduce the acceleration, velocity, displacement and other parameters of the sliding body. Therefore, accurate force histories from seismic inversions are crucial to estimate the landslide characteristics.

Some landslides have relatively simple evolutions, and basically slide as a whole with a nearly straight-line acceleration and deceleration process, for example the 2018 October 10 Baige landslide by the Jinsha river in Tibet (Sheng *et al.* 2020). However, there are

also many large-scale landslides with complex slipping processes and multiple subevents, which may not be described well by only one group of three-component force history. For example, the 2017 June 17 Nuugaatsiaq landslide in Greenland is mainly composed of two subevents, which are separated by ~50 s with a distance of ~1 km (Xie *et al.* 2020).

In addition, the period of a force history should be close to the duration of an acceleration–deceleration cycle of the bulk movement. It is not feasible to define a unified frequency range for all large-scale sliding events, which makes accurate filtering difficult. Signal filtering before waveform inversion may extract an incomplete signal or mix the signals from several subevents together. It would affect the accuracy of the force function and the analysis of the landslide motion characteristics.

At around 21:38 UT on 2017 June 23 (05:38 Beijing time on June 24), a catastrophic landslide occurred in the Fugui Mountains ($N32^{\circ}04'41''$, $E103^{\circ}39'40''$, at altitudes of 3100–3450 m) in the Xinmo village located in Maoxian County, Sichuan Province, China (Fig. 1). Villagers at the foot of the mountain were buried by $8 \times 10^6 \text{ m}^3$ rocks and soil, which resulted in 10 deaths and 73 missing (Fan *et al.* 2017a,b; Yin *et al.* 2017). The landslide destroyed more than 64 buildings, blocked approximately 2 km of the Songpinggou River, and damaged about 1 km of highway (Ouyang *et al.* 2017; Su *et al.* 2017). The landslide generated clear seismic waves that were

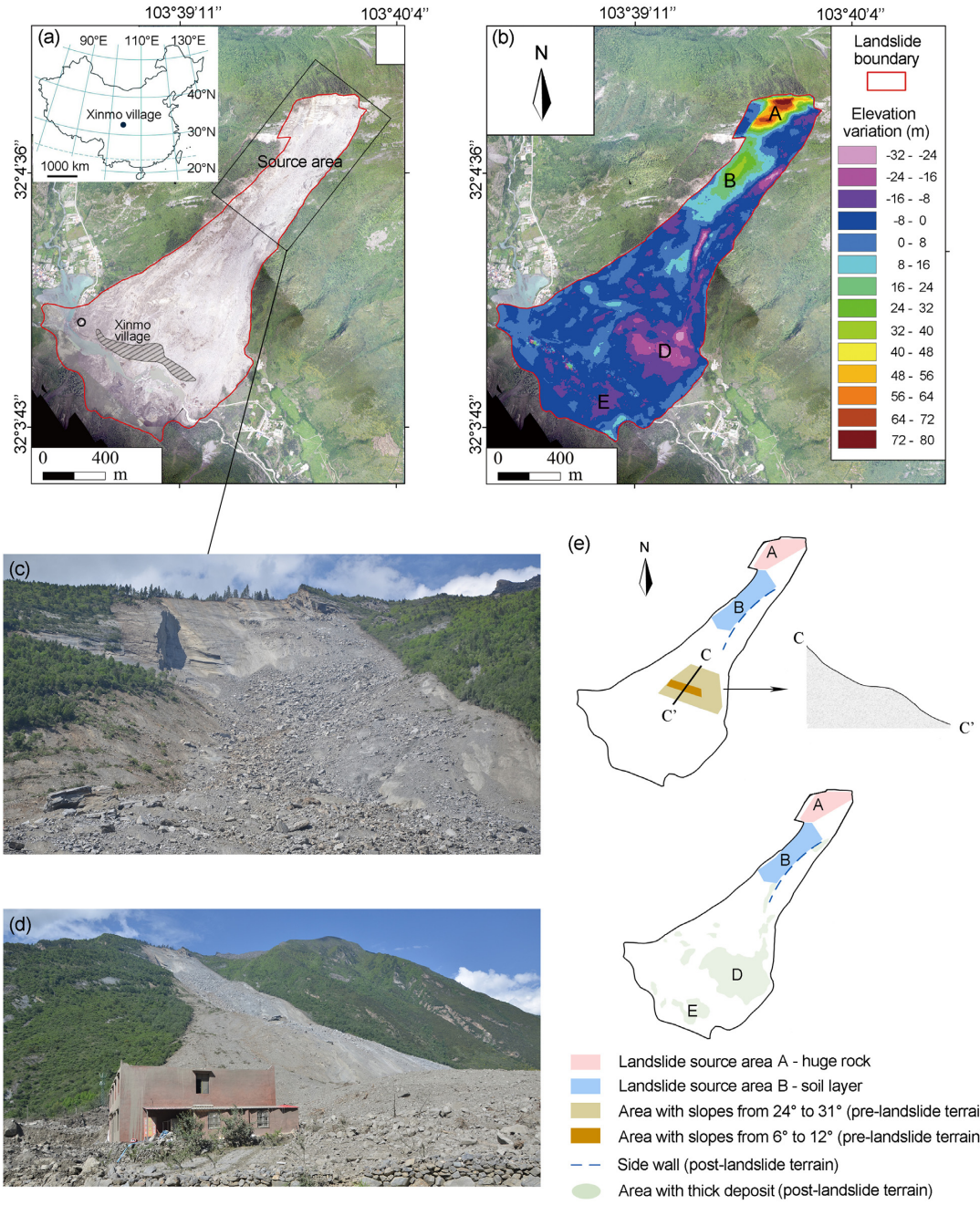


Figure 1. Field research results. (a) Post-landslide overview of Xinmo village (image taken by an UAV on 2017 June 25). The original location of the Xinmo village is marked by the black oblique lines, and the location of a two-story building is marked by the small black circle; (b) elevation variations estimated from the pre- and post-failure DEMs, and the two landslide source areas A and B; (c) photo of the landslide source area, (d) photo of a two-story building near the landslide boundary that was not buried during the landslide; (e) diagram of the pre- and post-landslide terrain features: the east sidewall in source area B, the hump with a gentle gradient (based on fig. 7 in Su et al. 2017), and the distribution of the landslide accumulation with a thickness of greater than 10 m (based on Fig. 1b in this study, fig. 4 in Fan et al. 2017a, fig. 1d in Ouyang et al. 2017 and fig. 5 in Su et al. 2017). In deposit area D, the deepest area is up to 26 m deep; while in deposit area E, the deepest area is up to 18 m deep.

recorded by the China National Seismic Network (CNSN, Fig. 2). These waveform data provide valuable insights for understanding the sliding processes.

In this study, first, we present the results from geological surveys of the Maoxian landslide and the seismic stations that recorded the data. Then, we perform a waveform inversion to obtain the force history. Before filtering the signals, we determine the frequency band of the effective signal by observing the broad-band

time–frequency plots of the inverted forces, and then, we split the three-component force history into several groups that define subevents during the Maoxian landslide. We believe that the terrain features, the characteristics of the deposit areas and other observations from field investigations may contribute to our understanding of landslide dynamics, and thus, we combine them with the subevent force histories to conduct a comprehensive analysis.

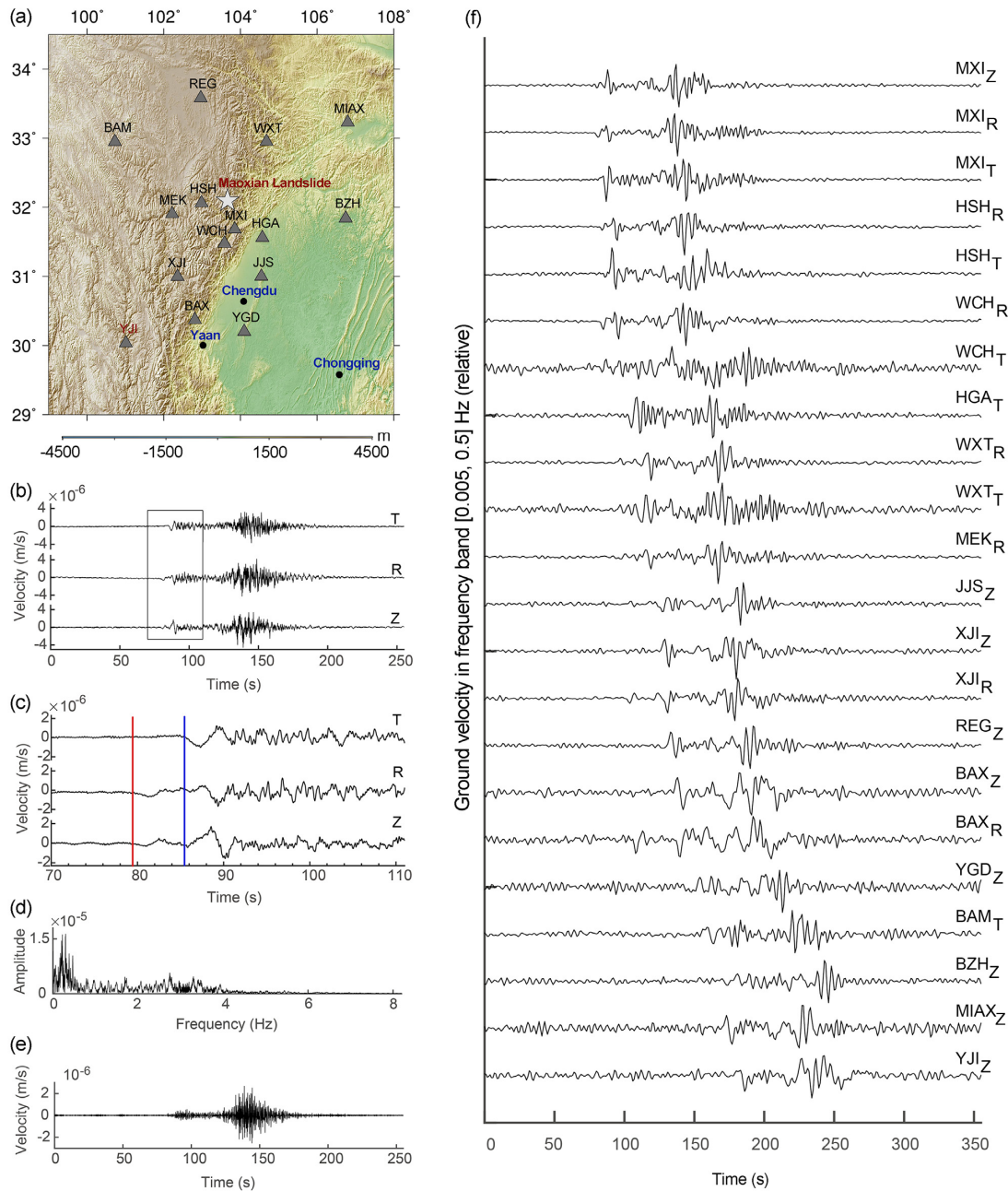


Figure 2. Seismic observation. (a) Seismic stations used in this study are designated by triangles; (b) three-component waveform recorded at station MXI; (c) P and S waves recorded at station MXI, the seismic waveform traces are aligned at the onset of the P waves (indicated by the red line), and the onset of the S waves (indicated by the blue line); (d) spectral analysis on the vertical velocity component at station MXI, (e) vertical velocity component in the 1–4 Hz frequency band at station MXI; and (f) the 22 seismic components collected from the 15 stations used in the inversion in the 0.005–0.5 Hz frequency band. Z, R and T refer to the vertical, radial and transverse components of the ground velocity, respectively. The Instrument response has been removed from all of the components.

2 DATA

2.1 Field investigation

The Maoxian landslide generally slipped towards the southwest with a total horizontal displacement of ~ 2200 m and a vertical displacement of ~ 1000 m, and covered a total area of $\sim 1 \times 10^6$ m 2 (see Fig. 1a). The maximum thickness of the deposit area was ~ 26 m, and the total volume was $\sim 8 \times 10^6$ m 3 . The elevation variations before and after the landslide are shown in Fig. 1(b).

The landslide materials primarily originated from two areas. Area A was a large $\sim 2.9 \times 10^6$ m 3 rock on the top of the mountain (Figs 1b and e), and area B was the soil layer downslope from the rock with a volume of $\sim 2.2 \times 10^6$ m 3 (Figs 1b and e). The gradient of the sliding bed under the soil layer is 24° – 31° , the gradient of the collapsed rock area is greater than 50° and the gradient of the deposit area is 10° – 18° (Ouyang *et al.* 2017; Su *et al.* 2017).

Based on the distribution of the local slope gradients before the landslide (fig. 7 in Su *et al.* 2017), the gradient in the middle of the sliding path becomes gentle and forms a hump. The elevation

variations (Fig. 1b) and photographic images of the landslide area (Fig. 1c) show sidewalls where the soil layer in source area B slid away. These important post- and pre-terrain features are labelled in Fig. 1(e).

2.2 Seismic observations

We obtained broadband seismic waveforms recorded by 15 stations from Data Management Center of CNSN (Data Management Centre of China National Seismic Network 2007, Zheng *et al.* 2010), which clearly show two arrivals (Figs 2a and b). Landslides exert a force on the Earth's surface and usually excite strong surface waves, with P waves hardly observed. However, the P wave generated by the Maoxian landslide can be identified on the waveform records at the closest station MXI with an epicentral distance of approximately 49 km (Fig. 2c). After rotation to radial and tangential components, the P wave is mostly on the radial and vertical components, and very weak on the tangential components. This is consistent with polarization of the longitudinal P waves. The differential traveltimes between surface and P waves is ~ 6 s, which is also consistent with the epicentral distance of 49 km, where the average S - and P -wave velocities of the crust are 3.55 and 6.1 km s^{-1} , respectively (Laske *et al.* 2013). From these observations, we can estimate origin time of a landslide subevent at around 05:38:51.5 (local time).

The MXI station is close to the landslide and can record high-frequency seismic energy (> 1 Hz). We conducted a spectral analysis of the vertical component at station MXI, and find that the high-frequency energy was mostly concentrated in the 1–4 Hz frequency band (Fig. 2d). Then, we use the vertical component bandpass filtered at 1–4 Hz as a reference to long-period forces in order to facilitate a combined analysis of force histories (Hibert *et al.* 2014). The correction for the propagation time was calculated following the method described by Hibert *et al.* (2017). The epicentral distance difference between the two stations was divided by the onset time difference of the short-period signals filtered between 1 and 4 Hz to obtain the average velocity of 2.6 km s^{-1} . At this velocity, it takes approximately 19 s for the 1–4 Hz seismic waves to travel to the station MXI.

Since some of the components (especially the horizontal components) of the seismic data at larger distances are seriously affected by noise, we only use 22 components (Fig. 2f) that have high signal-to-noise ratios at long periods for the inversion. These components are chosen from 15 stations with epicentral distances of 49–342 km (Fig. 2e).

3 METHODS

3.1 Waveform inversion

We invert to obtain the force history through deconvolution and solve the problem in the frequency domain, which effectively reduces the matrix dimensions during the calculation. We refer the readers to appendix A in Allstadt (2013) and section 3.2 in Zhao *et al.* (2015) for the details of the inversion method.

Since the exact frequency band of the force is unknown, we perform the inversion within a wide frequency range. We selected 800 s of data from each seismic station. This data and the Green's functions were bandpass filtered between 0.005 and 0.5 Hz using a Butterworth filter, and then, the data was downsampled to 2 samples per second. The Green's functions were generated using

the wavenumber integration method (Hermann 2002) based on the AK135 model (Kennett *et al.* 1995).

In order to determine the reliability of the inverted forces, we computed synthetic seismic waveforms by convoluting the inverted force with the Green's functions and comparing them with the real data. If the comparison is performed in the broad band of 0.01–0.2 Hz, it is difficult to see how well the two waveforms match in the lower frequency band, because the signal amplitude in the higher frequency band (0.036–0.2 Hz) is much larger than it is in the lower frequency band (0.01–0.036 Hz). Thus, we filtered the broad-band signals (both synthetic and real) in these two frequency bands for a better comparison (Fig. 3).

Short-period surface waves are very sensitive to small-scale heterogeneities in the Earth's crust, leading to inaccurate Green's function, which is calculated from a 1-D velocity model. Fortunately, the main energy after the inversion is concentrated in the low-frequency range (< 0.3 Hz), as can be seen from the time–frequency plots (Fig. 4c). Our analysis focuses on a frequency band lower than 0.2 Hz. The inversion errors in the higher frequency band do not affect the result in this frequency range.

The inversion operation is based on the point source single force model. A point source assumption requires that the wavelengths of the seismic waves used are much longer than the total displacement of the landslide (Fukao 1995). Allstadt (2013) elaborated on the feasibility of using seismic waves with a 30 s period to study the 2010 Mount Meager landslide mechanism, which had a sliding displacement of more than 12 km. In the Mount Meager area, the phase velocity of the ~ 30 s Rayleigh wave is $\sim 3.75\text{ km s}^{-1}$, while in the Maoxian area, the phase velocity of the ~ 5 s Rayleigh wave is approximately 3.55 km s^{-1} . Thus, it should be feasible to study the Maoxian landslide, which has a sliding displacement of approximately 2 km, by using the seismic waves with a 5 s period. Therefore, we include the 0.2 Hz seismic signals in the analysis of the Maoxian landslide and consider the signals at this frequency to be excited by the sliding of the mass. We analyse the reasonableness of this assumption later and consider other possible explanations.

We compare the inverted forces obtained from four inversion methods (Fig. 4b). Two of the inversion methods are carried out under the restriction of momentum conservation. From Fig. 4(b) and Tables 1 and 2, it can be seen that the waveform fitting degree of the four inverted forces is high. If the nature of a mechanical event is momentum conserved, the inverted force should be momentum conserved as long as the noise is filtered out correctly. The momentum conservation restriction of the inversion method is not necessary for all of the cases.

3.2 Separation in the frequency domain

We use time–frequency analysis to observe the change in the frequency content over time. This method has often been applied to seismic data generated by landslides (Moretti *et al.* 2012; Hibert *et al.* 2014; Zhao *et al.* 2015). In this study, we apply this method to the inverted force and observe the different subforces on the time–frequency plots. The time–frequency distribution of the different force energies was also observed by Sergeant *et al.* (2016) for icequakes (see their fig. 3).

The time–frequency plots of the waveform data from 2 stations (MXI and REG) are shown in Fig. 5, which can be compared with that of the inverted forces. The closer the station is to the landslide area, the more similar the seismic signal energy accumulation is to the inverted force. However, the energy of the signal observed in

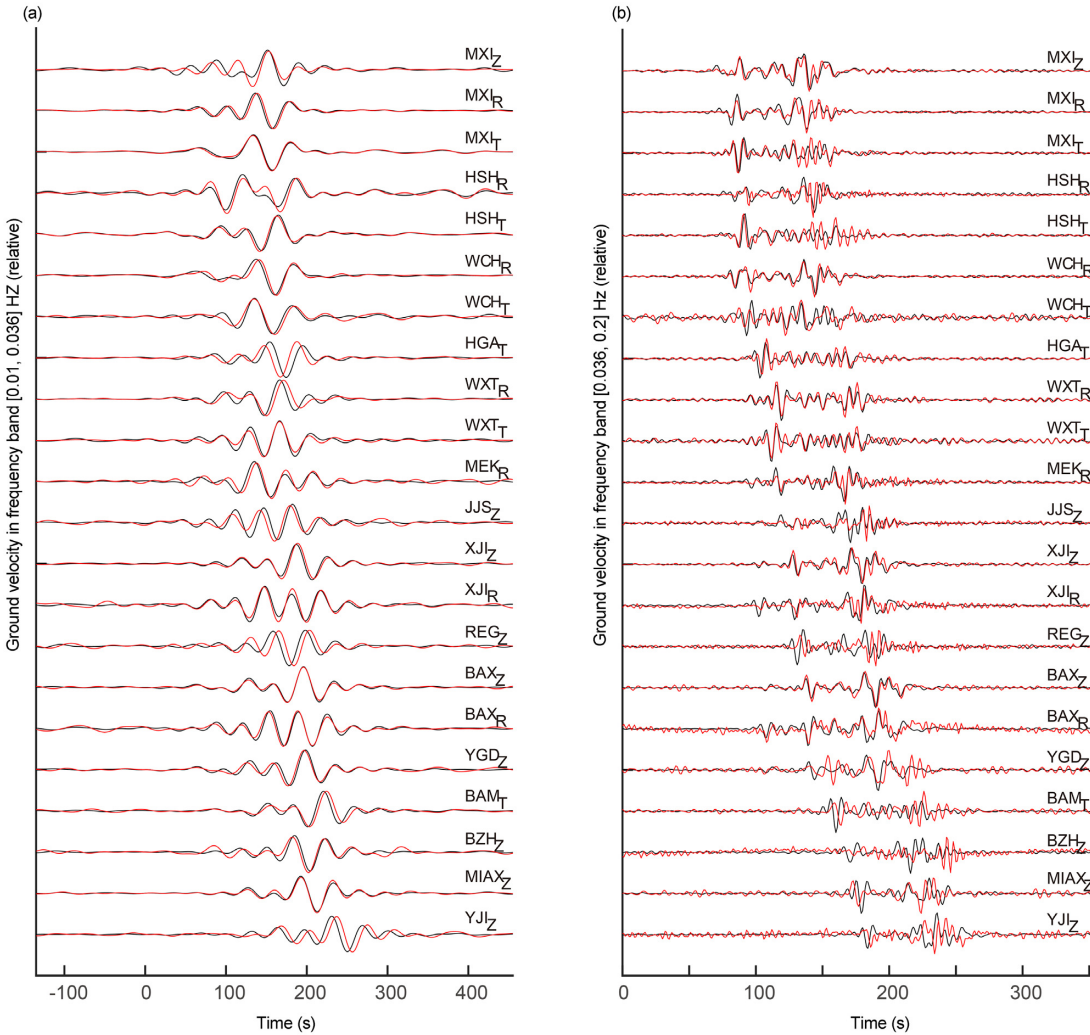


Figure 3. Comparison of the seismic records (black line) to the synthetic waveforms (red line) (a) in the frequency bands of 0.01–0.036 Hz and (b) in the frequency bands of 0.036–0.2 Hz.

the time–frequency plot is not proportional to the amplitude of the force generating it. The signals in the high-frequency band are much more visible. The signals associated with the low-frequency force, which are our key concern, are difficult to identify on the plots. The amplitude of the seismic signals is subject to the influences of many factors, so the time–frequency plot of the force (Figs 4c and 5a) is more reliable for the observation of the subevents.

To achieve the optimal time–frequency resolution, we used *S*-transform time–frequency analysis (Stockwell *et al.* 1996) to generate the plots. In Figs 4(c) and 5(a), we observe the energy of the persistent low-frequency noise below 0.01 Hz, which is especially significant in the horizontal components, and the energy of the landslide subevents around the observation time of the landslide. Thus, the force function can be extracted using a band–pass filter with a lower cut-off frequency of 0.01 Hz.

In all of the figures, the origin of the time axis corresponds to 05:37:40 local time. It was decided according to the start times of the effective long-period forces (Fig. 4b) and the start times of the energy accumulation on the time–frequency plots of the forces (Figs 4c and 5a).

According to the energy concentrations, we segment the force into four parts (Fig. 4c). However, it should be noted that not all

of the subevents can be directly separated. Each part in the time–frequency plot may still include several events that occur successively in time and within a similar frequency range. For this reason, further division is needed.

3.3 Separation in the time domain

When a sliding body accelerates while moving downwards or decelerates while moving upwards along the slope, the direction of the vertical ground force F_Z is upward. When the sliding mass decelerates while sliding downwards, the direction of F_Z is downward (see Fig. 6a). Assuming a straight-line motion, we can use the azimuth of the horizontal force F_H to determine the motion direction, and the acceleration and deceleration stages (Allstadt 2013; Yamada *et al.* 2013). If the landslide motion track projected on the horizontal plane is a curve, both centripetal acceleration and acceleration along the tangent line occur. At this moment, F_H is the resultant force of the two acceleration vectors. The force and the change in the azimuth of the horizontal force are relatively complex. The azimuth does not directly correspond to the direction of motion; however, the change in the azimuth indicates whether the sliding mass is moving clockwise or counterclockwise. When

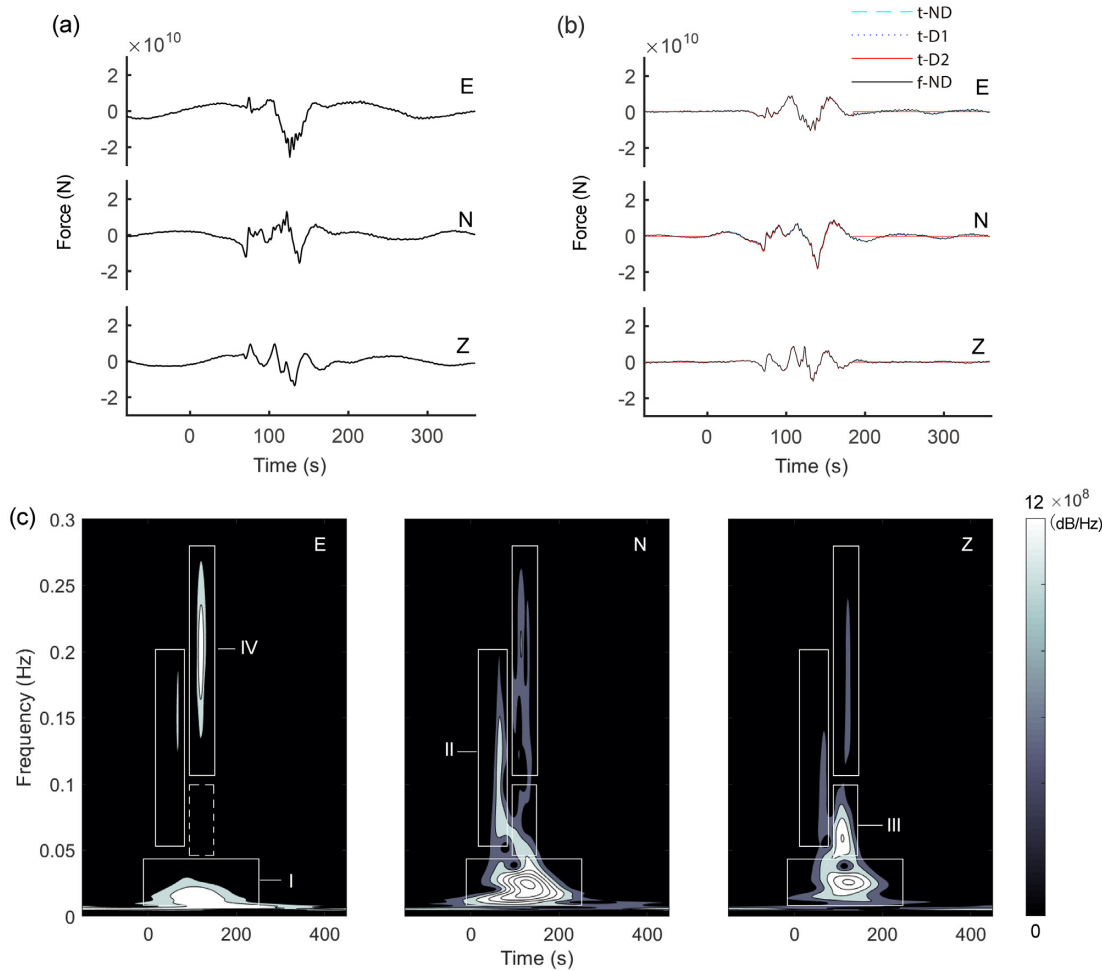


Figure 4. Inversion results and subevent separation in the frequency domain. (a) Inverted forces in the 0.005–0.5 Hz frequency band. The inversion problem is solved in the frequency domain. (b) Comparison of the inverted forces in the 0.01–0.2 Hz frequency band obtained from four inversion methods: the first method is to invert in the time domain without the momentum conservation restriction (t-ND); the second method is to invert in the time domain with the constraint that all of the components of the single force must add up to zero (t-D1); the third method is basically the same as the second method, but the momentum conservation restriction is applied in the period of 0–183 s (t-D2); the fourth method is to invert in the frequency domain in the 0.005–0.5 Hz frequency band without the momentum conservation restriction, and then, filter the force in the 0.01–0.2 Hz frequency band (f-ND). (c) *S*-transform time–frequency analysis of the inverted forces in the 0.005–0.5 Hz frequency band. The force histories are segmented into four parts: the time interval of part I is 0–220 s and its frequency range is 0.01–0.04 Hz; part II is from 40 to 85 s and has a frequency range of 0.05–0.2 Hz; parts III and IV are both from 100 s to 140 s, but have frequency ranges of 0.04–0.1 and 0.1–0.3 Hz, respectively. E, N and Z refer to the east–west, north–south and vertical components, respectively.

Table 1. Rmse between t-D2 and the other three inversion forces.

	f-ND (10^8 N)	t-ND (10^8 N)	t-D1 (10^8 N)
E	2.06	1.14	1.48
N	6.52	5.25	4.64
Z	1.76	0.54	0.41

Table 2. *R*-squared values between t-D2 and the other three inversion forces.

	f-ND	t-ND	t-D1
E	0.9970	0.9991	0.9985
N	0.9895	0.9932	0.9947
Z	0.9969	0.9997	0.9998

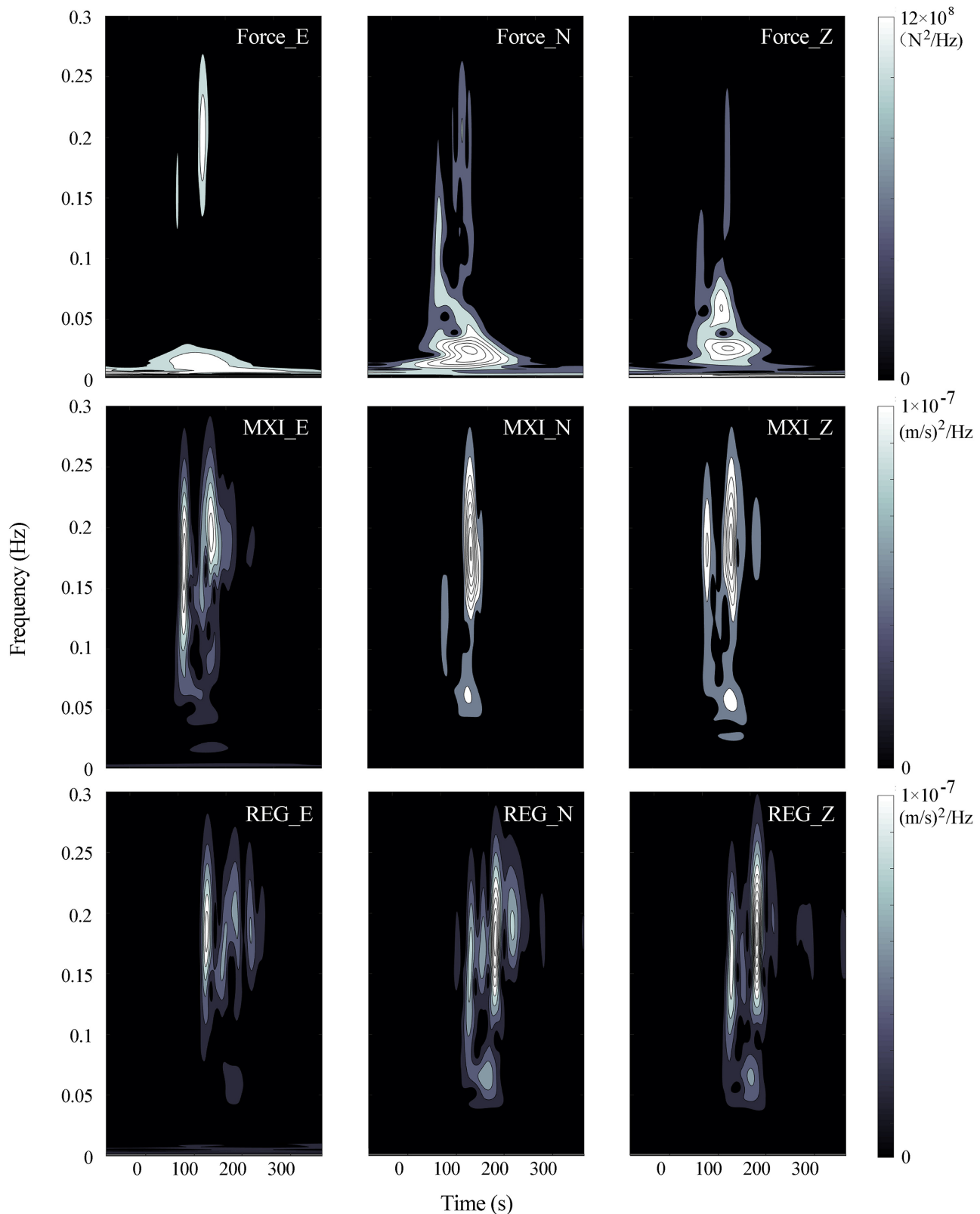
the sliding body is moving with a uniform circular motion on the horizontal plane, the change in the horizontal azimuth is regular (Fig. 6b).

When the landslide begins, the sliding body accelerates downward. As can be seen in Fig. 6(a), the vertical component of the

force on the ground is upward. Therefore, we can define the starting time of an event as when the vertical component of the force passes the zero and becomes positive (Fig. 7). Then, based on the starting point, we can determine whether the sliding body moves in a straight line or along a curve and whether it accelerates or decelerates based on the azimuthal change in the horizontal force.

$$F = Mg(\sin \theta - \mu \cos \theta). \quad (1)$$

If the sliding mass accelerates in a straight line, we can compare it with the ideal situation when the bulk mass slides down the slope. In this case, the tangent of the slope angle θ is the ratio between the vertical and horizontal variations in the force (Zhao *et al.* 2015). Taking the joint force as F , it is possible to calculate the weight of the sliding mass M using eq. (1) and to estimate the landslide volume V when the density is known. We set the density of the mass as 2600 kg m^{-3} . The empirical formula of Lucas *et al.* (2014), $\mu = V^{-0.0774}$, gives the friction coefficient values of between 0.36 and 0.29 for volumes of 0.5×10^6 to $8 \times 10^6 \text{ m}^3$. The decrease in



Downloaded from https://academic.oup.com/gji/article-abstract/222/3/1965/5850368 by INFU BIBLIO PLANETS user on 21 July 2020

Figure 5. Time–frequency plots in the 0.003–0.5 Hz frequency band of the inverted force, the seismic waveforms at station MXI and REG. E, N and Z refer to the east–west, north–south and vertical components, respectively.

the friction with increasing volume can explain the seismic signals that are generated by rockfalls (Levy *et al.* 2015) or large landslides (Yamada *et al.* 2018). To facilitate the calculation, we set μ as 0.3 according to Yamada *et al.* (2016, 2018) who studied landslides

with volumes of 2×10^6 to $8 \times 10^6 \text{ m}^3$. In our calculation, the sliding mass may travel slightly further and have a faster speed than if we use the formula of Lucas *et al.* (2014). However, this does not affect the final conclusions.

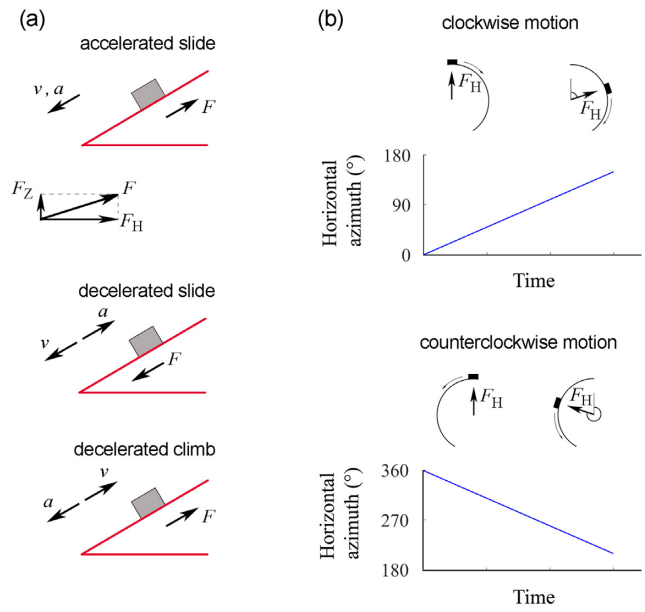


Figure 6. Characteristics of block movement. (a) Relationship between the block motion along the slope and the joint ground force direction, and (b) change in the horizontal azimuth when the block moves in a uniform circular motion on the horizontal plane.

When we calculate M and F , the acceleration, the velocity and the displacement of the sliding mass are also known (Brodsky et al. 2003; La Rocca et al. 2004; Allstadt 2013; Ekström & Stark 2013; Yamada et al. 2013; Hibert et al. 2014; Zhao et al. 2015).

If the calculated sliding path of a subevent stops continuing forward at a certain time, or if it presents an anomalous reversion trend, it is considered to be the end of the event (see the calculated displacement in Figs 8b and c). Then, the next zero crossing point of the vertical component is defined as the start of the following event. Thus, the four parts of the frequency domain can be divided further.

4 RESULTS

4.1 Landslide subevents

We obtain eight subevents, which are numbered chronologically (see Figs 7a–d and 9). We also perform more precise filtering after this division (see the third column in Table 3). The parameters of the motion characteristics of the subevents are shown in Table 3. The dipping angle $\theta = \tan^{-1} \frac{F_Z}{F_H}$ is calculated when the joint force has the maximum value in the (nearly) straight-line acceleration stage. We use the values of F and θ at this moment to calculate M using eq. (1), assuming a constant mass during the sliding process to complete the subsequent calculations of the acceleration, velocity and displacement.

Except for the parameters of subevent 4, which has a completely curvilinear motion during the acceleration stage, all of the values in Table 3 were calculated based solely on the force histories. The signal frequency of subevent 8 is relatively high (>0.1 Hz), and it includes almost no straight-line motion (Fig. 7d). We could not make a further division or estimate the mass.

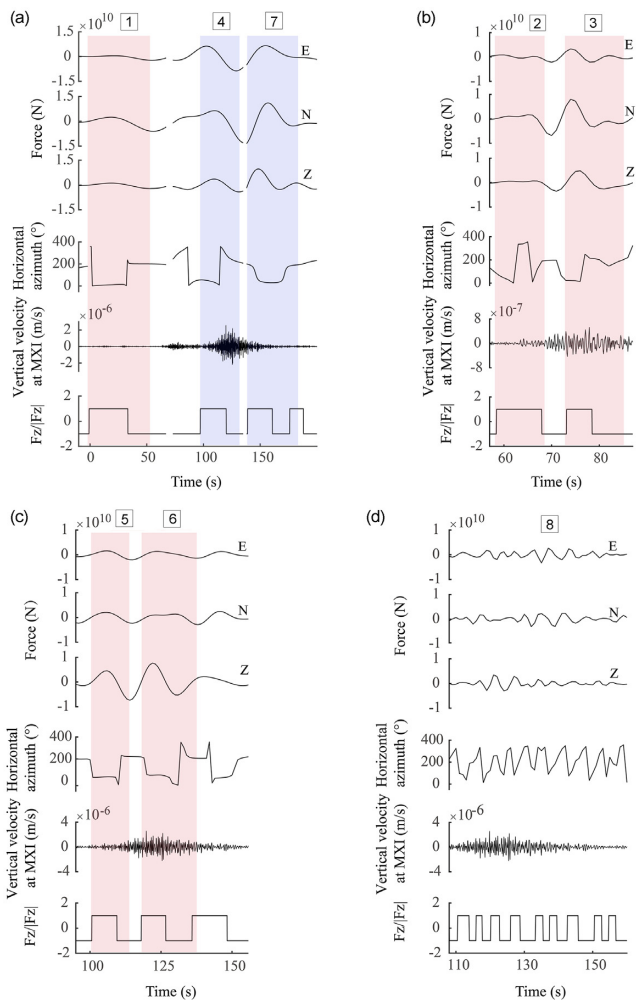


Figure 7. Three-component force histories, horizontal ground force azimuths, vertical ground velocity at station MXI, and vertical ground force directions (upward is positive) of (a) subevent 1 in the 0.01–0.02 Hz frequency band, subevents 4 in the 0.01–0.03 Hz frequency band, and subevent 7 in the 0.01–0.036 Hz frequency band; (b) subevents 2 and 3 in the 0.05–0.15 Hz frequency band; (c) subevents 5 and 6 in the 0.036–0.1 Hz frequency band; and (d) subevent 8 in the 0.1–0.3 Hz frequency band.

4.2 Landslide process

The Maoxian landslide occurred in a tectonically active region. Several recent studies (Ouyang et al. 2017; Su et al. 2017; Yin et al. 2017) have interpreted the Maoxian landslide based on field investigations. They determined that first, the earthquake-fractured bedded rock mass at the top of the mountain slide down (source area A in Fig. 1b), and then, it entrained and transported a large amount of debris along its run. We provide a more detailed interpretation of the landslide by combining the existing field investigation with the force histories from the seismic inversion.

Subevents 2, 3, 5 and 6 in the higher frequency band have short durations and displacements, independent analysis does not reveal the locations where they occurred. However, we can acquire useful information if they are placed in the time chain of all of the subevents. Therefore, we put them aside and will reevaluate these events after analysing the three main subevents (1, 4 and 7) in the lowest frequency band.

Since we know that the rock sliding preceded the sliding of the soil layer, the start of the sliding path of subevent 1 should be

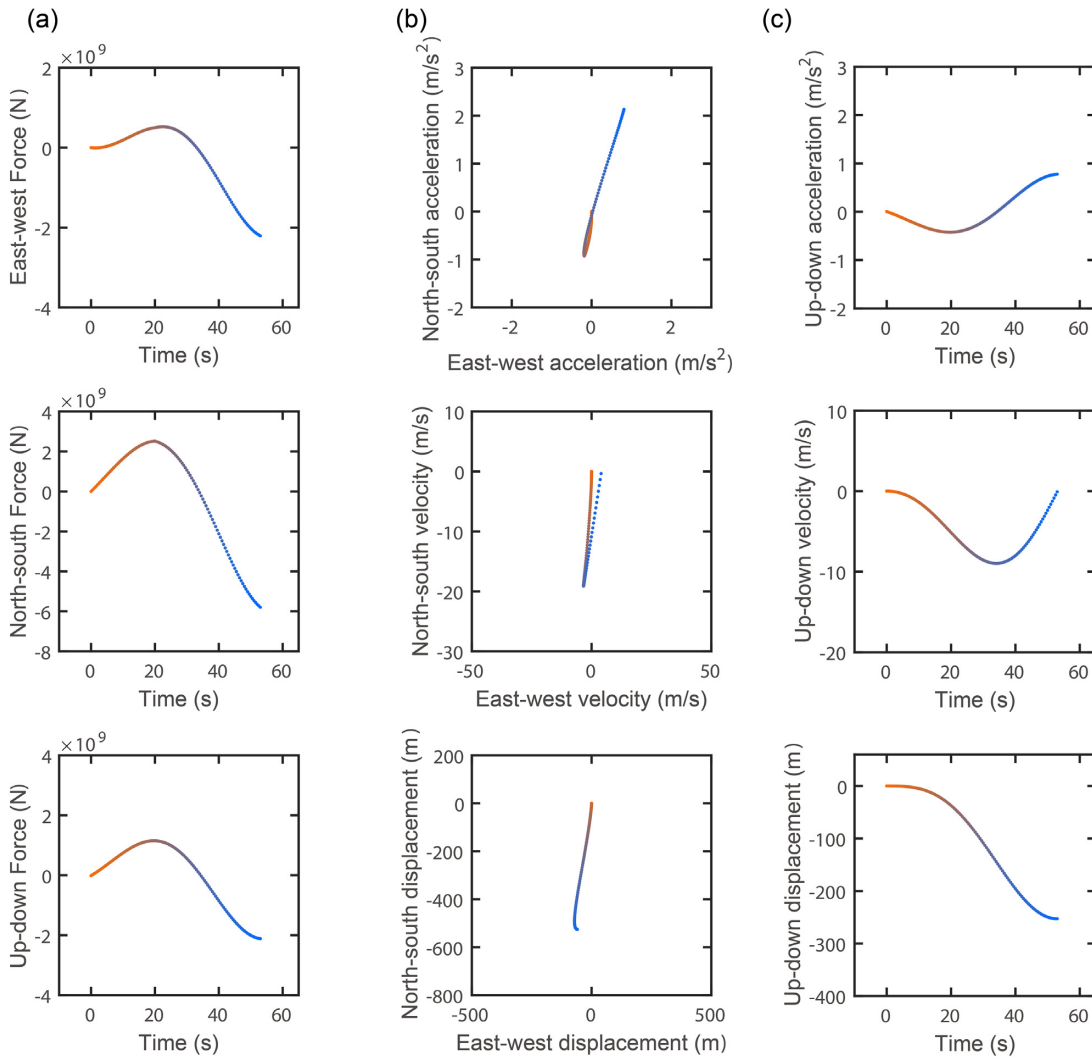


Figure 8. Calculation results for subevent 1, dots are plotted for each 0.5 s of time. (a) Force functions during the duration of subevent 1. Acceleration, velocity and displacement of subevent 1 (b) on the horizontal plane and (c) in the vertical direction.

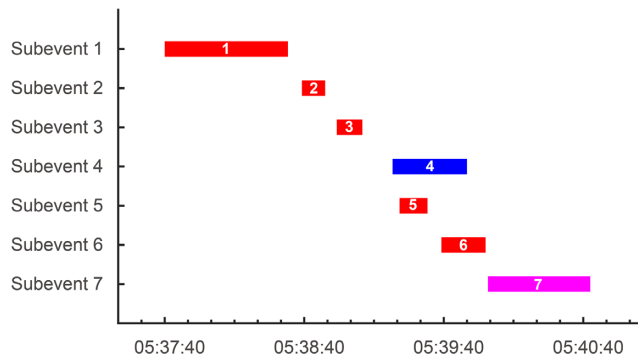


Figure 9. Time sequence diagram of the landslide subevents according to the fourth column in Table 3.

located in landslide source area A where the rock was originally located. The calculated horizontal displacement is 528 m. Deposit was observed at the end of its path (Fig. 10a); however, this is not the main deposition site. Most of the mass in subevent 1 continued to slide after the calculated end point, but this process is not reflected in the force in the [0.01, 0.02] Hz frequency band. This is likely due

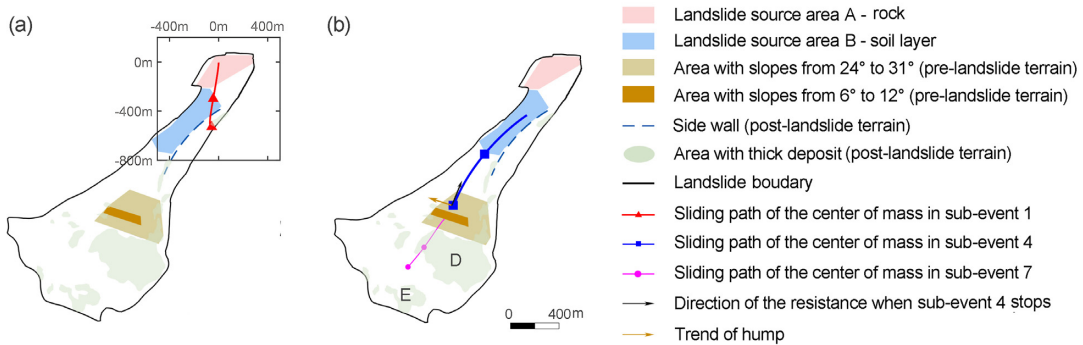
to a change in the frequency band or the presence of broken sliding bodies.

As can be seen from Fig. 7(a), the change in the azimuth of the horizontal force between 98 and 130 s implies that the sliding mass moves counterclockwise during subevent 4. These changes are similar to those shown in Fig. 6(b). The sidewalls (Figs 1e and 10) may cause the path of the huge sliding mass to curve. This kind of curvilinear motion due to the restriction of the terrain has also been found by Allstadt (2013) and Moretti *et al.* (2015). Then, we assume that subevent 4 occurred in source area B, where initially half of the soil layer moves from the location where the elevation variations in Fig. 1b is largest, and then, it gradually increases to the full volume of 2.2×10^6 m³, which is the result of erosion. The calculated sliding path fits well with the terrain and terminates before the hump in the slide path, and the direction of the resistance force applied by the ground is almost perpendicular to the trend of the hump (see Fig. 10b).

The horizontal azimuth of subevent 7 (139–150 s in Fig. 7a) shows that initially, it decelerates, and then, it accelerates. Combined with the upward vertical force (139–150 s in Fig. 7a), we determine that the process involves an initial decelerated climb followed by an accelerated slide (Fig. 6a). Since the sliding path

Table 3. Parameters of the landslide subevents.

Subevents	Assigned number in first division	Frequency range (Hz)	Sliding duration (s)	θ ($^{\circ}$)	M (10^{10} kg)	V (10^6 m 3)	Horizontal displacement (m)	Vertical displacement (m)	Maximum velocity (m s $^{-1}$)
1	I	[0.01, 0.02]	(0, 53)	24	0.272	1.047	528	252	21.4
2	II	[0.05, 0.15]	(59, 69)	24	0.121	0.465	40	21	7.9
3	II	[0.05, 0.15]	(74, 85)	30	0.380	1.460	34	29	6.6
4	I	[0.01, 0.03]	(98, 130)		0.572	2.200	672	284	39.6
5	III	[0.036, 0.1]	(101, 113)	59	0.075	0.287	181	244	38.2
6	III	[0.036, 0.1]	(119, 138)	62	0.0845	0.325	211	397	40.3
7	I	[0.01, 0.036]	(139, 183)	25	1.270	4.886	502	235	16.7
8	IV	[0.1, 0.3]							

**Figure 10.** Diagram of the pre- and post-landslide terrain features showing the sliding paths of the subevents. (a) Sliding path of subevent 1 and (b) sliding paths of subevents 4 and 7.

of subevent 4 terminates before the hump, we consider merging subevents 4 and 7 together. Namely, the soil layer in area B slides, and then, it is impeded by its encounter with the hump. The mass slows down and accumulates before the hump, after which it climbs over the hump and finally breaks through the obstacle and resumes sliding.

In the later decelerating phase of subevent 4 (Fig. 7a), the vertical component of the high-frequency seismogram at station MXI shows an apparent high energy (high amplitude). A likely explanation for this is that the severe crushing of the sliding body radiates high-frequency energy. When the motion in subevent 7 changes from the decelerated climb to the accelerated slide, that is, when the azimuth of the horizontal force in Fig. 7(a) changes by approximately 180°, the high-frequency energy decreases because the crushing towards the obstacles is alleviated. When the mass is severely fractured due to its interaction with the obstacle, we cannot calculate the displacement of subevent 4 using eq. (1) because at this time, the inverted force does not only apply to the mass of subevent 4. In addition, due to the existence of this process, there is a gap between the sliding paths of subevents 4 and 7.

The velocity of the sliding body when it has just crossed the top of the hump is unknown. Assuming that the velocity is 0 m s $^{-1}$, the calculated sliding path of subevent 7 crosses deep deposit area D (Fig. 10b). The actual displacement should be longer and could reach another thick deposit area at the bottom of the landslide boundary (deposit area E in Fig. 10b). The volume of the sliding mass in subevent 7 is close to the total volume of soil in the landslide (see Table 3), and it can be regarded as the result of continuously scraping the slide bed.

Similar to subevent 1, subevents 2 and 3 occur before the soil layer slides, so their sliding paths can also start in the source area A. Since subevent 2 occurs after subevent 1 and its volume is smaller than that of subevent 1, it is also possible that subevent 2 is the followup of subevent 1.

Subevents 5 and 6 occur seven seconds after the soil layer starts to slide. At this time, the landslide has completely launched. The forces generated by subevents 5 and 6 can only be distinguished from the force of subevent 4 when they occur outside of source area B. The calculated slopes of the two subevents are greater than 50° (see Table 3), which is identical to the post-slide terrain in landslide source area A. Thus, subevents 5 and 6 are determined to be the sliding of the remaining part of the rock on the summit. The sum of the volumes of subevents 1, 2, 3, 5 and 6 is approximately 3.58×10^6 m 3 , which is very close to the volume of rock in the landslide source area A (Ouyang et al. 2017; Su et al. 2017).

After the overall consideration of the time sequence in Fig. 9 and the parameters in Table 3, we conclude that the process of the Maoxian landslide is as follows: the landslide began at 05:37:40 (local time), rock masses with volumes of approximately 1×10^6 , 0.5×10^6 and 1.5×10^6 m 3 slide in sequence, which caused the soil layer underneath the rock, as well as the remaining rock mass to slide at 05:39:18. The sliding mass was obstructed at the halfway point by the hump, and then, it underwent significant fracturing and continuous accumulation, after which it soon overcame the obstacle and slide in a southwest direction. The mass decelerated again when it reached the gently sloping deposition area, after which it finally stopped.

5 DISCUSSION

Our method of separating the landslide subevents first separates the low-frequency noise and the effective force based on the time–frequency plots. We consider the energy below 0.01 Hz to be from the low-frequency noise. However, we do not rule out the possibility that the landslide also produces forces below 0.01 Hz, which are mixed with the low-frequency noise. In this case, the force history is not completely recovered. Ekström & Stark (2013) showed that

the duration of the landslide motion is related to the maximum force F_{\max} obtained from the inversion. For the Maoxian landslide, F_{\max} was approximately 3.5×10^{10} N, an acceleration–deceleration cycle should be less than 75 s according to Figs 2(e) and (f) in Ekström & Stark (2013). In addition, the results of the numerical simulation (Ouyang *et al.* 2017) show that a continuous sliding from source area A to the deposit area is completed within 100 s. Even if there is landslide information in the frequency band below 100 s, ignoring this information does not significantly impact our analysis.

When extracting independent subforce functions from signals that overlap in time and space, we use the block model and assume constant friction μ . Yamada *et al.* (2016) estimated the friction of the Akatani landslide, and concluded that the landslide accelerated rapidly in the beginning; the coefficient of friction soon reached a steady state; for a given volume, the average dynamic coefficient of friction throughout the entire landslide movement can be taken as a constant. This result is consistent with the results of other studies (Lucas *et al.* 2014; Moretti *et al.* 2015). We assume that the coefficient of friction μ and the volume of the sliding body are both constant values during each subevent. According to eqs (1), the change in F is only dependent on the change in the slope angle θ . When θ decreases and μ is greater than the $\tan(\theta)$, F becomes negative and the sliding enters the deceleration stage until it stops (see fig. 9b in Levy *et al.* 2015 e.g.). Since θ is unlikely to increase again, F will not return to 0 when the sliding body stops moving. Thus, when the force function of each subevent terminates, it does not return to zero (Figs 7 and 8a) as a sinusoidal function would. However, in the process of each subevent, the constant mass of the sliding body starts with a velocity of 0 and ends with a velocity of approximately 0. The entire process also conforms to the law of momentum conservation.

Before the ending stage of an actual landslide, the sliding body has already broken into pieces and sometimes has changed into debris flows. In the Maoxian landslide case, the block model is no longer suitable to study the movement in the ending stage. This is the limitation of our methods and expected to be solved in future studies.

Compared with the force amplitude of subevents 4 and 7, the force amplitude of subevent 1 is low, and there is no corresponding representation in the high-frequency signal at station MXI. Generally, the waveform of subevent 1 should be considered to be noise and ignored. However, we think it is still likely to be an effective force function. If the landslide volume is small, or the landslide is far from the station, the high-frequency seismic wave generated by the landslide may not be received. However, this does not indicate that there are no high-frequency signals generated. In addition, high-frequency signals attenuate faster than low-frequency signals during wave propagation. Therefore, it is possible that the high-frequency signals may not be seen, while the low-frequency forces are observed after inversion.

In Fig. 4(c), there is an obvious energy accumulation in the 0.01–0.02 Hz frequency band from 0 to 100 s on the north–south plot. In Fig. 3(a), the horizontal components of the seismic waves from several nearby stations (MXI, HSH and WCH) show low-frequency information corresponding to the force from 0 to 60 s. According to our calculations (Fig. 8), the horizontal velocity and the vertical velocity of subevent 1 reduce to 0 (i.e. the mass stops moving forward/downward), at nearly the same time. We also found a correspondence between the horizontal displacement (528 m), the vertical displacement (252 m) and the landslide's topography. We believe that this result is too coincidental for subevent 1 to be noise.

Subevents 2, 3, 5 and 6 are in the higher frequency band of 0.036–0.2 Hz. We explain them using the single force sliding

theory as we did in the lower frequency band. The force histories of these subevents have short durations, and have short sliding distances (horizontal displacements of <220 m, see Table 3). This is most likely because the large rock broke into smaller pieces, which followed their own independent paths (like individual rocks fall) during sliding, and thus, could not be treated as a bulk mass and could not be identified from the inverted force even if they continued to slide downward. In previous studies, the seismic wave periods for studying the sliding mechanism of a landslide are generally longer than 10 s. So, the ~0.2 Hz signals could also be related to some other retrogressive or progressive failures in the complex landslide process. However, even if they are completely irrelevant to the sliding, this will not affect the main conclusion that we have drawn from the lower frequency band.

6 CONCLUSIONS

First, we inverted the seismic waveforms to obtain the three-component force histories of the landslide over a wide frequency band. By considering the force energy concentration on the time–frequency plots, subevents that in different frequency bands and in different time intervals were separated. The events with close frequency bands and that occurred in succession were further isolated in the time domain.

By analysing the force histories of the subevents, we determined their motion parameters and estimated their sliding paths. Using the topographic features, characteristics of the deposition area, and the other conclusions drawn from the field survey, we located the starting point of each sliding path and clarified the correlation among the various subevents. This is a new method for the integrated use of landslide observation technologies. The result is also conducive to the numerical simulation of complicated landslides.

In our future research, we aim to locate the landslide subevents more accurately using two approaches: the first approach is to improve the location accuracy by installing seismometers in the landslide region to record continuous seismic noises, which can be used to extract reliable Green's function along each path by noise correlations (Levshin *et al.* 2012). The second one is to track the sliding mass using back projection methods of seismic records from dense seismic networks, similar to the way in which the rupture front of an earthquake is resolved (Koper *et al.* 2011).

ACKNOWLEDGEMENTS

We are grateful to Eleonore Stutzmann, Lijun Su, Jun Xie, Bingxin Shi and Changrong He for useful discussions. We also thank two anonymous reviewers for their useful comments to improve our manuscript. We used generic mapping tools to draw the figures (Wessel & Smith 1991). Waveform data for this study are provided by Data Management Centre of China National Seismic Network at Institute of Geophysics (SEISDMC, doi:10.11998/SeisDmc/SN), China Earthquake Networks Center and GS, QH, SC, SN Seismic Networks, China Earthquake Administration. The website is <http://www.seisdmc.ac.cn/>. This work was supported by National Natural Science Foundation of China (no. 4150020346) and by the ERC contract ERCCG–2013–PE10–617472 SLIDEQUAKES.

REFERENCES

- Allstadt, K., 2013. Extracting source characteristics and dynamics of the August 2010 Mount Meager landslide from broadband seismograms, *J. geophys. Res.—Earth.*, **118**(3), 1472–1490.

- Brodsky, E.E., Gordeev, E. & Kanamori, H., 2003. Landslide basal friction as measured by seismic waves, *Geophys. Res. Lett.*, **30**(24), 2236, doi:10.1029/2003GL018485.
- Data Management Centre of China National Seismic Network, 2007. *Waveform Data of China National Seismic Network*. Institute of Geophysics, China Earthquake Administration, doi:10.11998 /SeisDmc/SN, <http://www.seisdmc.ac.cn>.
- Ekström, G. & Stark, C.P., 2013. Simple scaling of catastrophic landslide dynamics, *Science*, **339**, 1416, doi:10.1126/science.1232887.
- Fan, J.R., Zhang, X.Y., Su, F.H., Ge, Y.G., Paolo, T., Yang, Z.Y., Zeng, C. & Zeng, Z., 2017a. Geometrical feature analysis and disaster assessment of the Xinmo landslide based on remote sensing data, *J. Mt. Sci.—Engl.*, **14**(9), 1677–1688.
- Fan, X.M. et al., 2017b. Failure mechanism and kinematics of the deadly June 24th 2017 Xinmo landslide, Maoxian, Sichuan, China, *Landslides*, **14**, 2129–2146.
- Farin, M., Mangeney, A., De Rosny, J., Toussaint, R. & Trinh, P.T., 2018. Insights into the generated seismic signal and dynamics of granular flows on horizontal and sloping beds, *J. geophys. Res.—Earth*, **123**(6), 1407–1429.
- Favreau, P., Mangeney, A., Lucas, A., Crosta, G. & Bouchut, F., 2010. Numerical modeling of landquakes, *Geophys. Res. Lett.*, **37**, L15305, doi:10.1029/2010GL043512.
- Fukao, Y., 1995. Single force representation of earthquakes due to landslides or the collapse of caverns, *Geophys. J. Int.*, **122**, 243–248.
- Gualtieri, L. & Ekström, G., 2018. Broad-band seismic analysis and modeling of the 2015 Taan Fjord, Alaska landslide using Instaseis, *Geophys. J. Int.*, **213**(3), 1912–1923.
- Hermann, R.B., 2002. *Computer Programs in seismology, An Overview of Synthetic Seismogram Computation, Version 3.30*. Department of Earth and Atmospheric Sciences, Saint Louis University, Available at: <http://www.eas.slu.edu/eqc/eqc-cps/CPS/CPS330.html>, last accessed September 20, 2017.
- Hibert, C., Ekström, G. & Stark, C.P., 2014. Dynamics of the Bingham Canyon Mine landslides from seismic signal analysis, *Geophys. Res. Lett.*, **41**, 4535–4541.
- Hibert, C., Stark, C.P. & Ekström, G., 2015. Dynamics of the Oso–Steelhead landslide from broadband seismic analysis, *Nat. Hazard. Earth. Sys.*, **15**(6), 1265–1273.
- Hibert, C., Ekström, G. & Stark, C.P., 2017. The relationship between bulk-mass momentum and short period seismic radiation in catastrophic landslides, *J. geophys. Res.—Earth*, **122**(5), 1201–1215.
- Iverson, R.M. et al., 2015. Landslide mobility and hazards: implications of the 2014 Oso disaster, *Earth Planet Sci. Lett.*, **412**, 197–208.
- Kanamori, H. & Given, J.W., 1982. Analysis of long-period seismic waves excited by the May 18, 1980, eruption of Mount St. Helens—a terrestrial monopole? *J. geophys. Res.*, **87**(B7), 5422–5432.
- Kawakatsu, H., 1989. Centroid single force inversion of seismic-waves generated by landslides, *J. geophys. Res.*, **94**(B9), 12 363–12 374.
- Kennett, B.L.N., Engdahl, E.R. & Buland, R., 1995. Constraints on seismic velocities in the Earth from travel times, *Geophys. J. Int.*, **122**, 108–124.
- Koper, K.D., Hutko, A.R., Lay, T., Ammon, C.J. & Kanamori, H., 2011. Frequency-dependent rupture process of the 2011 Mw 9.0 Tohoku Earthquake: comparison of short-period P wave backprojection images and broadband seismic rupture models, *Earth Planet Space*, **63**(7), 599–602.
- La Rocca, M., Galluzzo, D., Saccrotti, G., Tinti, S., Cimini, G.B. & Pezzo, E.D., 2004. Seismic signals associated with landslides and with a tsunami at Stromboli Volcano, Italy, *Bull. seism. Soc. Am.*, **94**(5), 1850–1867.
- Laske, G., Masters, G., Ma, Z. & Pasyanos, M., 2013. Update on CRUST1.0: a 1-degree global model of earth's crust, *Geophys. Res. Abstr.*, **15**, Abstract EGU2013–2658.
- Levshin, A.L., Barmin, M.P., Moschetti, M.P., Mendoza, C. & Ritzwoller, M.H., 2012. Refinements to the method of epicentral location based on surface waves from ambient seismic noise: introducing Love waves, *Geophys. J. Int.*, **191**(2), 671–685.
- Levy, C., Mangeney, A., Bonilla, F., Hibert, C., Calder, E.S. & Smith, P.J., 2015. Friction weakening in granular flows deduced from seismic records at the Soufrière Hills Volcano, Montserrat, *J. geophys. Res.—Sol. Earth*, **120**, 7536–7557.
- Li, Z.Y., Huang, X.H., Xu, Q., Yu, D., Fan, J.Y. & Qiao, X.J., 2017. Dynamics of the Wulong landslide revealed by broadband seismic records, *Earth Planet Space*, **69**, 27, doi:10.1186/s40623–017–0610–x.
- Li, Z.Y., Huang, X.H., Yu, D., Su, J.R. & Xu, Q., 2019. Broadband-seismic analysis of a massive landslide in southwestern China: dynamics and fragmentation implications, *Geomorphology*, **336**(2019), 31–39.
- Lin, C.H., Kumagai, H., Ando, M. & Shin, T.C., 2010. Detection of landslides and submarine slumps using broadband seismic networks, *Geophys. Res. Lett.*, **37**(22), L22309, doi:10.1029/2010GL044685.
- Lucas, A., Mangeney, A. & Ampuero, J.P., 2014. Frictional velocity-weakening in landslides on Earth and on other planetary bodies, *Nat. Commun.*, **5**, 3417, doi:10.1038/ncomms4417.
- Moretti, L., Allstadt, K., Mangeney, A., Capdeville, Y., Stutzmann, E. & Bouchut, F., 2015. Numerical modeling of the Mount Meager landslide constrained by its force history derived from seismic data, *J. geophys. Res.—Sol. Earth*, **120**, 2579–2599.
- Moretti, L., Mangeney, A., Capdeville, Y., Stutzmann, E., Huggel, C., Schneider, D. & Bouchut, F., 2012. Numerical modeling of the Mount Steller landslide flow history and of the generated long period seismic waves, *Geophys. Res. Lett.*, **39**, L16402, doi:10.1029/2012GL052511.
- Ouyang, C.J., Zhao, W., He, S.M., Wang, D.P., Zhou, S., An, H.C., Wang, Z.W. & Cheng, D.X., 2017. Numerical modeling and dynamic analysis of the 2017 Xinmo landslide in Maoxian County, China, *J. Mt. Sci.—Engl.*, **14**(9), 1701–1711.
- Schöpa, A., Chao, W.A., Lipovsky, B.P., Hovius, N., White, R.S., Green, R.G. & Turowski, J.M., 2018. Dynamics of the Askja caldera July 2014 landslide, Iceland, from seismic signal analysis: precursor, motion and aftermath, *Earth Surf. Dynam.*, **6**(2), 467, doi:10.5194/esurf-6-467-2018.
- Sergeant, A., Mangeney, A., Stutzmann, E., Montagner, J.P., Walter, F., Moretti, L. & Castelnau, O., 2016. Complex force history of a calving-generated glacial earthquake derived from broadband seismic inversion, *Geophys. Res. Lett.*, **43**(3), 1055–1065.
- Sheng, M., Chu, R., Wang, Y. & Wang, Q., 2020. Inversion of source mechanisms for single-force events using broadband waveforms, *Seismol. Res. Lett.*, **91**(3), 1820–1830, doi:10.1785/0220190349.
- Stockwell, R.G., Mansinha, L. & Lowe, R.P., 1996. Localization of the complex spectrum: the S transform, *IEEE Trans. Signal Process.*, **44**(4), 998–1001.
- Su, L.J. et al., 2017. Characteristics and triggering mechanism of Xinmo landslide on 24 June 2017 in Sichuan, China, *J. Mt. Sci.—Engl.*, **14**(9), 1689–1701.
- Xie, J., Chu, R. & Ni, S., 2020. Relocation of the June 17th, 2017 Nuugaatsiaq (Greenland) landslide based on Green's functions from ambient seismic noises, *J. geophys. Res.—Sol. Earth*, **125**, e2019JB018947, doi:10.1029/2019JB018947.
- Wessel, P. & Smith, W., 1991. Free software helps map and display data, *EOS, Trans. Am. geophys. Un.*, **72**(441), 445–446.
- Yamada, M., Kumagai, H., Matsushi, Y. & Matsuzawa, T., 2013. Dynamic landslide processes revealed by broadband seismic records, *Geophys. Res. Lett.*, **40**, 2998–3002.
- Yamada, M., Mangeney, A., Matsushi, Y. & Moretti, L., 2016. Estimation of dynamic friction of the Akatani landslide from seismic waveform inversion and numerical simulation, *Geophys. J. Int.*, **206**, 1479–1486.
- Yamada, M., Mangeney, A., Matsushi, Y. & Matsuzawai, T., 2018. Estimation of dynamic friction and movement history of large landslides, *Landslides*, **15**, 1963–1974.
- Yin, Y.P., Wang, W.P., Zhang, N., Yan, J.K. & Wei, Y.J., 2017. The June 2017 Maoxian landslide: geological disaster in an earthquake area after the Wenchuan Ms 8.0 earthquake, *Sci. China Technol. Sci.*, **60**, 1762–1766.
- Zhao, J. et al., 2015. Model space exploration for determining landslide source history from long period seismic data, *Pure appl. Geophys.*, **172**(2), 389–413.
- Zheng, X.F., Yao, Z.X., Liang, J.H. & Zheng, J., 2010. The role played and opportunities provided by IGP DMC of China National Seismic Network in Wenchuan earthquake disaster relief and researches, *Bull. seism. Soc. Am.*, **100**(5B), 2866–2872.